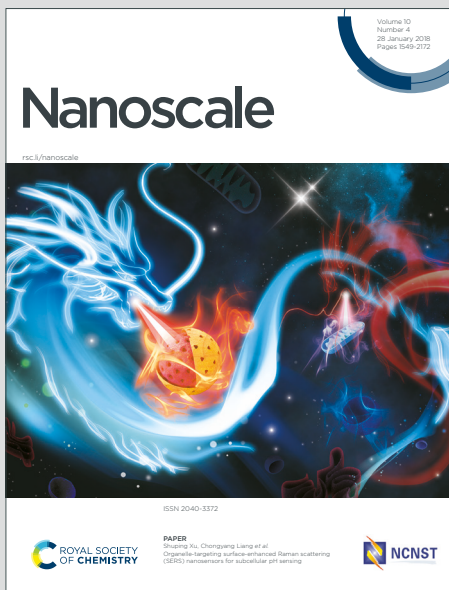


Nanoscale

Accepted Manuscript

This article can be cited before page numbers have been issued, to do this please use: D. Weng, C. Ling, J. He, Q. Cui, C. Xu and B. Gu, *Nanoscale*, 2026, DOI: 10.1039/D5NR04405G.



This is an Accepted Manuscript, which has been through the Royal Society of Chemistry peer review process and has been accepted for publication.

Accepted Manuscripts are published online shortly after acceptance, before technical editing, formatting and proof reading. Using this free service, authors can make their results available to the community, in citable form, before we publish the edited article. We will replace this Accepted Manuscript with the edited and formatted Advance Article as soon as it is available.

You can find more information about Accepted Manuscripts in the [Information for Authors](#).

Please note that technical editing may introduce minor changes to the text and/or graphics, which may alter content. The journal's standard [Terms & Conditions](#) and the [Ethical guidelines](#) still apply. In no event shall the Royal Society of Chemistry be held responsible for any errors or omissions in this Accepted Manuscript or any consequences arising from the use of any information it contains.

Multifunctional nonlinear photonic devices based on spatial self-phase modulation in InP nanosheets

Danyi Weng,^a Cheng Ling,^a Jun He,^b Qiannan Cui,^{a,*} Chunxiang Xu,^{a,*} and Bing Gu^{a,*}

^a *School of Electronic Science & Engineering, Southeast University, Nanjing 211198, China*

^b *School of Physics and Electronics, Central South University, Changsha 410012, China*

* qiannan@seu.edu.cn

* xcxseu@seu.edu.cn

* gubing@seu.edu.cn

Abstract

Indium phosphide (InP) has high carrier mobility and excellent optoelectronic properties, demonstrating significant potential for applications in optical communications and photodetectors. Its two-dimensional (2D) nanosheets exhibit unique optical nonlinearity due to quantum confinement effects, yet their third-order nonlinear optical properties remain rarely explored. In this work, we prepare and characterize InP nanosheet dispersions, investigate their spatial self-phase modulation (SSPM) behaviors, and demonstrate their applications in multifunctional nonlinear photonic devices. By studying the ring formation dynamics of SSPM patterns, the ring formation time τ_F and the third-order nonlinear susceptibility of monolayer InP nanosheets $\chi_{\text{monolayer}}^{(3)}$ are measured to be about 0.3 s and 10^{-9} esu, respectively. The formation mechanism of SSPM primarily arises from the interaction between coherent light and InP nanosheets. Leveraging the superior electronic coherence and photostability of InP nanosheets, four types of nonlinear photonic devices are designed and demonstrated, including all-optical switches, spatially asymmetric light transmitters, photonic diodes, and optical logic gates. This work not only bridges a critical gap in third-order nonlinear optical research of III-V semiconductor



nanomaterials, but also pioneers new avenues for developing high-performance multifunctional nonlinear photonic devices.

Keywords: multifunctional nonlinear photonic devices, InP nanosheets, spatial self-phase modulation, nonlinear optical effect

1. Introduction

Over the past two decades, III-V compound semiconductors have demonstrated tremendous application prospects in developing high-performance optoelectronic devices, such as lasers,^[1] photodetectors,^[2] modulators,^[3] solar cells,^[4] light-emitting diodes,^[4] and single-photon emitters,^[5] owing to their unique electrical and optical properties.^[6] Among them, indium phosphide (InP) is an extremely attractive direct-bandgap III-V semiconductor with ultra-high electron mobility of $4800 \text{ cm}^2 \text{ V}^{-1} \text{ s}^{-1}$ at room temperature,^[7] which is approximately three times that of silicon ($1450 \text{ cm}^2 \text{ V}^{-1} \text{ s}^{-1}$).^[8] This characteristic endows it with exceptional applications in near-infrared band optoelectronic devices. For instance, Chen *et al.*^[9] employed Zn diffusion technique to achieve high responsivity in planar InP/InGaAs/InP photodetectors at 1310 nm and 1550 nm. Jain *et al.*^[10] developed avalanche photodetectors based on InP/InAsP nanowires, demonstrating 12-fold gain at 1550 nm. Recently, Zhang *et al.*^[11] reported superior electrical performance in InGaAs/InP photodetectors and investigated their charge transport processes.

Beyond its exceptional optoelectronic properties, InP's remarkable nonlinear optical properties have also attracted significant research interest. As early as 1995, Dvorak *et al.*^[12] characterized the nonlinear refractive index ($\sim 10^{-12} \text{ cm}^2 \text{ W}^{-1}$) of bulk InP at 1064 nm using Z-scan measurements. In 2007, Wang *et al.*^[13] demonstrated that InP nanocrystals exhibit strong the nonlinear optical properties, with a nonlinear refractive index ($\sim 10^{-9} \text{ cm}^2 \text{ W}^{-1}$) three orders of magnitude greater than that of bulk InP. Most recently in 2020, Liu *et al.*^[6] reported superior nonlinear absorption properties of InP nanowires and their application as saturable absorbers for ultrafast laser pulse generation. In short, InP nanostructures exhibit diverse forms, including nanocrystals,

nanowires, and nanosheets. It is well documented that the optical nonlinearity of InP strongly depends on its nano-structural configuration.^[6,13] Notably, two-dimensional (2D) nanosheets—owing to quantum confinement effects—localize electrons within the planar dimension, manifesting unique optical nonlinearity.^[14] However, studies on third-order nonlinear optical effects in InP nanosheets remain rarely reported to date.

Spatial self-phase modulation (SSPM) refers to a phenomenon where an intense laser beam transmitted through a third-order nonlinear optical sample generates concentric multi-ring patterns in the far field.^[15,16] Due to its simple experiments, intuitive results, and convenient calculations, SSPM has emerged as a prevalent technique for characterizing nonlinear optical properties of emerging 2D nanomaterials, including violet phosphorus (VP),^[17] SnS,^[18] graphene oxide (GO),^[19] $Ti_3C_2T_x$,^[20] and Ga_2Te_3 .^[21] Meanwhile, SSPM based on novel materials has enabled the development of diverse passive nonlinear photonic devices, such as all-optical switches,^[14] photonic diodes,^[22] optical isolators,^[23] information converters,^[18] logic gates,^[24] spatially asymmetric light transmitters,^[25] etc. Specifically, Wu *et al.*^[14] reported a dual-wavelength all-optical switch using MoS_2 nanosheets. Nayak *et al.*^[26] demonstrated all-optical modulations and photonic diodes based on SSPM in porphyrin-naphthalimide molecules. Weng *et al.*^[25] developed both the spatially asymmetric light propagation and all-optical switching based on SSPM of semimetal MoP microparticles. Wu *et al.*^[23] designed all-optical logic OR gates and optical isolators using 1D@0D hybrid dimensional heterojunction. Notably, Xu *et al.*^[24] ingeniously constructed an integrated and reconfigurable multifunctional all-optical logic gate, achieving nine basic Boolean logic functions in a single configuration. In a word, researchers have developed single- or dual-function nonlinear photonic devices based on the excellent SSPM of diverse nanomaterials. Nevertheless, with the continuous emergence of novel optical materials, traditional single-function devices fail to meet the demand for integration and multifunctionality in future intelligent photonic chips. Consequently, there is an urgent need to develop multifunctional nonlinear photonic devices based on unified material platforms—for instance, utilizing SSPM in a single material to simultaneously achieve all-optical switching, wavelength conversion, and logic gates—thereby overcoming



View Article Online
https://doi.org/10.1039/D5NR04405G
current device limitations and advancing next-generation photonic integration technologies.

In this work, we prepared InP nanosheets, studied their SSPM phenomena, and demonstrated their multifunctional nonlinear photonic device applications. By measuring the ring formation dynamics of SSPM patterns, the ring formation time τ_F and the third-order nonlinear susceptibility of monolayer InP nanosheets $\chi_{\text{monolayer}}^{(3)}$ were obtained, and the underlying SSPM formation mechanism was analyzed. Furthermore, leveraging the superior electronic coherence and photostability of InP nanosheets, four types of nonlinear photonic devices were designed and demonstrated, including all-optical switches using InP nanosheets, spatially asymmetric light transmitters in InP/GO, photonic diodes using InP/SnS₂, and optical logic gates based on InP nanosheets.

2. Preparation and characterization of InP nanosheets

2.1 Preparation of InP nanosheets

In the presented work, all samples were prepared using the ultrasonic method, known for its simplicity and widespread application, which facilitates the large-scale exfoliation and dispersion of 2D nanomaterials in solvents.^[27] Bulk InP was purchased from Meryer (Shanghai) Biochemical Technology Co., Ltd. as the raw material. The bulk InP was ground and sieved, then 60 mg of the processed material was ultrasonically treated for 450 min in 30 mL of 1-methyl-2-pyrrolidone (NMP) solution. During the entire ultrasound process, the temperature was maintained below 30 °C to prevent material oxidation. After standing for 12 hours, the resulting dark gray suspension separated into two distinct layers: the supernatant and the precipitate. The supernatant was collected for subsequent material characterization and SSPM measurements. To determine the mass concentration d_0 of the supernatant, the precipitate was rinsed and dried at 85 °C for 10 hours. After weighing, 56.2 mg of InP was obtained, thereby revealing that the supernatant contained 3.8 mg of InP. Therefore, the mass concentration of InP nanosheets dispersed in NMP solution was calculated to



be $d_0 = 0.127 \text{ mg mL}^{-1}$.

2.2 Material characterization

To characterize the as-prepared InP nanosheets, we conducted the following analyses: Morphology was characterized using a Zeiss GeminiSEM 360 scanning electron microscope (SEM); Crystal structure was determined with a Rigaku Smartlab 9 X-ray diffractometer (XRD); Molecular vibration signatures were recorded on a Horiba Scientific LabRAM HR Evolution Raman spectrometer; The topography and thickness distribution were mapped via a Bruker Dimension Icon atomic force microscope (AFM); Linear absorption spectrum of InP nanosheets in NMP solution was measured employing a Shimadzu 3600 Plus UV-Vis-NIR spectrophotometer.

2.3 Characterization results

Figure 1(a) shows the SEM image of the as-prepared InP nanosheets, which indicates that larger number of InP crystal are successfully exfoliated into nanosheets via the ultrasonic method. As shown in Fig. 1(b), the XRD pattern of InP nanosheets exhibits three prominent diffraction peaks at $2\theta = 26.2^\circ$, 43.5° , and 51.5° , indexed to the (111), (220), and (311) planes of the zinc blende-structured InP (reference PDF #73-1983),^[28] confirming the typical zinc blende crystal of the as-prepared samples. The significantly reduced peak intensity at $2\theta = 26.2^\circ$ can be attributed to the decrease in crystallinity of the nanosheets. Figure 1(c) displays the Raman spectrum of InP nanosheets. Two distinct characteristic peaks are observed at 304 cm^{-1} and 344 cm^{-1} , which are assigned to the transverse optical and longitudinal optical modes, respectively. It is noteworthy that the transverse optical peak position of the InP nanosheets coincides with that of InP nanowires, while the longitudinal optical peak is completely consistent with that of bulk InP.^[29] Figures 1(d) and 1(e) present the AFM image of InP nanosheets and corresponding thickness distribution statistics, respectively. Since the influence of SSPM is almost independent of the lateral size of the 2D nanosheets^[17-20], here we only focus on the thickness of InP nanosheets. Analysis of the red Gaussian fitting curve in Fig. 1(e) yields an average nanosheet thickness of 2.1 nm. This value corresponds to

the theoretical thickness of monolayer InP nanosheets and shows excellent agreement with literature reports.^[17] Figure 1(f) shows the UV-Vis-NIR absorption spectrum of InP nanosheets in NMP solution, revealing weak absorption across the broad spectral range. The optical bandgap of InP nanosheets is determined as $E_g = 1.38$ eV using Tauc's formula $(\alpha_0 h\nu)^2 = \text{const } (h\nu - E_g)$,^[30] where α_0 denotes the linear absorption coefficient and $h\nu$ represents the photon energy. The inset in Fig. 1(f) presents the corresponding Tauc plot, demonstrating the linear relationship between $(\alpha_0 h\nu)^2$ and $h\nu$. The E_g value is measured to be 1.38 eV, which is in close agreement with reported ones.^[31,32]

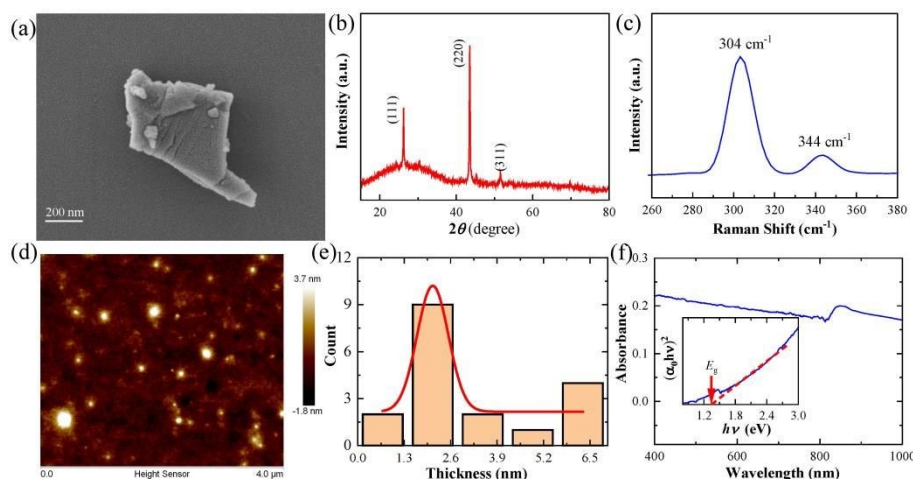


Figure 1. Characterization of InP nanosheets. (a) SEM image, (b) XRD pattern, and (c) Raman spectrum of as-prepared InP nanosheets. (d) AFM image of InP nanosheets with (e) corresponding thickness distribution statistics. (f) UV-vis-IR absorption spectrum of InP nanosheets in NMP solution; the inset is $(\alpha_0 h\nu)^2$ versus $h\nu$.

3. Nonlinear optical properties of InP nanosheets

3.1 SSPM experiments

Based on the advantages of simple experiments, intuitive results, and convenient calculations, the SSPM has been extensively employed for characterizing the third-order nonlinear refractive index of diverse nanomaterials.^[15,16] In the SSPM experiments, two different wavelengths of fundamental Gaussian laser beams with wavelengths of $\lambda = 532$ nm (green light) and $\lambda = 671$ nm (red light) are served as light



sources. The nonlinear optical sample consists of InP nanosheets with a mass concentration of $d_0 = 0.127 \text{ mg mL}^{-1}$ dispersed in NMP solution and placed in a quartz cuvette with a thickness of $L = 10 \text{ mm}$. The combination of a half-wave plate and a Glan-Taylor prism (G-T) is used to precisely control the laser power incident on the sample. The laser beam is focused onto the sample through a convex lens with a focal length of $f = 400 \text{ mm}$, and its waist radii on the focal plane are estimated to be $77.0 \mu\text{m}$ at $\lambda = 532 \text{ nm}$ and $68.9 \mu\text{m}$ at $\lambda = 671 \text{ nm}$, respectively. The back surface of the cuvette is positioned 30 mm before the focal plane. Ultimately, the formation dynamics of the self-diffraction ring patterns could be monitored on a white screen or a camera located 150 mm from the back surface of the sample.

3.2 Dynamic of formation SSPM

In the SSPM experiment, we recorded the dynamic evolution of the far-field self-diffraction ring of InP nanosheets dispersed in NMP solution under different intensities I with respect to the laser irradiation time t (defined as the time delay at the start of laser irradiation). Figure 2(a) displays the evolution of a representative self-diffraction ring pattern over time t at $I = 205.5 \text{ W cm}^{-2}$. It is shown that the dynamic formation process of SSPM rings can be decoupled into three stages, namely (i) Ring growth stage: the initial circular spot evolves into a concentric multi-ring structure, the ring size continues to expand and the number of rings increases until a complete self-diffraction ring is formed, at which time the number of self-diffraction rings reaches its maximum N_{\max} and the outermost ring radius reaches its maximum R_{\max} ; (ii) Ring collapse stage: under the influence of gravity driven thermal convection, the upper half of the complete self-diffraction ring collapses towards the center; (iii) Steady state stage: the distorted ring structure approaches a time-invariant steady state. This dynamic process can quantify two characteristic time parameters: (i) the ring formation time τ_F , which is defined as the time interval from the start of laser irradiation to the formation of a complete self-diffraction ring; (ii) the ring collapse time τ_C , which is the time interval between the complete self-diffraction ring evolving into a steady-state distorted ring. As shown in Fig. 2(a), we yield the maximum number of rings $N_{\max} = 14$, the ring formation time τ_F



[View Article Online](#)
 = 0.32 s, and the ring collapse time $\tau_C = 1.21$ s for InP nanosheets dispersed in NMP solution at $I = 205.5 \text{ W cm}^{-2}$. The measured τ_F value is comparable to those of ~ 0.37 s of VP nanosheets^[17] and ~ 0.38 s of MoP microparticles^[25].

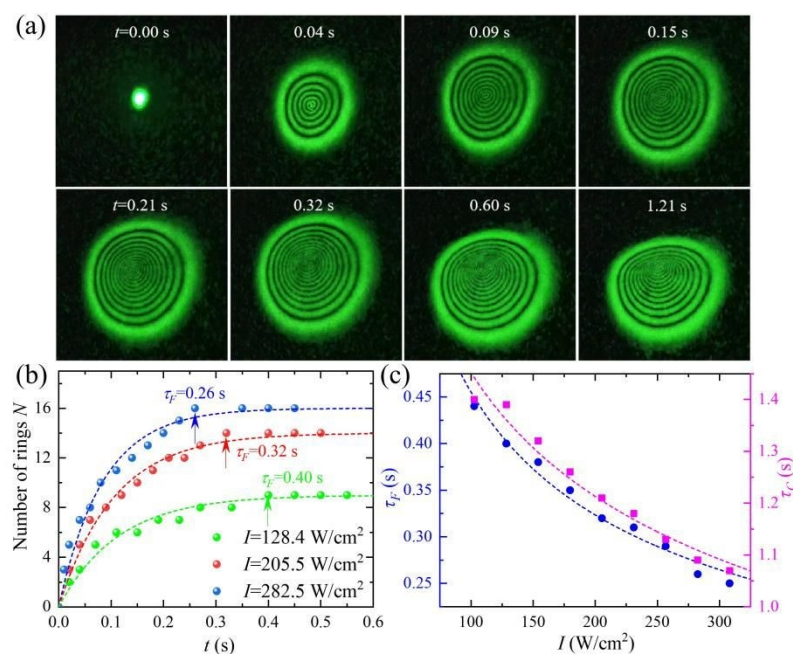


Figure 2. Dynamics of ring formation in SSPM patterns. (a) The SSPM patterns of InP nanosheets dispersed in NMP at different time t with $I = 205.5 \text{ W cm}^{-2}$. (b) The evolution of the ring number N over time t at three representative intensities I . (c) The formation time τ_F and collapse time τ_C of the ring under different intensities I .

Figure 2(b) illustrates the evolution of the number of self-diffraction rings N over time t at three representative intensities of $I = 128.4, 205.5$, and 282.5 W cm^{-2} . The experimental results show that the number of rings N increases nonlinearly with time t and gradually saturates, eventually approaching a constant value. This dynamic behavior is governed by $N(t) = N_{\max} [1 - \exp(-t / \tau_R)]$, where τ_R denotes the characteristic rise time for self-diffraction ring formation. In Fig. 2(b), the dashed lines represent the optimal fitting curves of the measured $N(t)$ - t data, from which the characteristic rise time τ_R at intensities $I = 128.4, 205.5$, and 282.5 W cm^{-2} are obtained as 0.113, 0.106, and 0.084 s, respectively. Concurrently, the ring formation times τ_F measured at $I = 128.4, 205.5$, and 282.5 W cm^{-2} are 0.40, 0.32, and 0.26 s, respectively.



Figure 2(c) presents the dependence of both ring formation time τ_F and ring collapse time τ_C on the laser intensity I . It is shown that the experimentally measured τ_F values exhibit an inverse proportionality to the intensity I , consistent with previous reports.^[14,17,25,33,34] Similarly, the measured τ_C values also inversely proportional to the intensity I . The above phenomenon can be recapitulated as follows: the higher the intensity, the faster the nonlinear optical response, resulting in a significant reduction in the formation time of self-diffraction rings and thereby a markedly accelerated collapse process. Next, the physical mechanism behind this phenomenon will be described in detail.

3.3 Formation mechanism of SSPM

The dynamics of formation SSPM in InP nanosheet suspensions originates from the physical mechanism of coherent light-nanosheet interactions, which we briefly analyze below. The optical bandgap of InP nanosheets is $E_g = 1.38$ eV, while the incident photon energy $h\nu = 2.33$ eV at $\lambda = 532$ nm or 1.85 eV at 671 nm in the experiments resides in the non-parabolic region of their band structure. Owing to the high electron mobility of InP up to 4800 $\text{cm}^2 \text{V}^{-1} \text{s}^{-1}$ at room temperature,^[7,35] intense laser irradiation induces a significant population of valence-band electrons in InP nanosheets to absorb photons and undergo transitions to the conduction band. Driven by the optical electric field, the intense laser beam induces polarization and reorientation of InP nanosheets dispersed in NMP solution through an energy-relaxation mechanism. The coherent interplay between the Gaussian beam and reoriented InP nanosheets enhances the phase modulation effect, leading to a progressive increase in self-diffraction ring number over time (see Fig. 2(a)). Within this process, the SSPM phenomenon originates from nonlocal electron coherent interaction between incident laser beam and InP nanosheets. The formation dynamics of SSPM in NMP-suspended InP nanosheets can be physically interpreted using the wind-chime model.^[14] Beyond the laser-induced electron coherence that dominates the formation of self-diffraction ring patterns, the thermal effect also contributes partially to the SSPM process—as evidenced by the collapse of the upper self-diffraction ring segment at $t = 0.60$ s in Fig. 2(a), which arises from



gravity-driven thermal convection in the solution. Consequently, the primary physical origin of light-InP interactions in the SSPM phenomenon is laser-induced electron coherence, with thermal effect constituting a secondary contribution.

3.4 Nonlinear optical characterization of InP suspensions

At a fixed laser intensity, the SSPM ring formation dynamics yield a complete self-diffraction ring pattern (e.g., Fig. 2(a)), enabling measurement of the maximum number of rings N_{\max} . By systematically varying intensity I and repeating the SSPM experiments, we obtain the N_{\max} values across different intensities at 532 nm and 671 nm wavelengths, with results presented in Figs. 3(a) and 3(b). Note that we repeat each SSPM experiment three times and obtain similar experimental results, which proves the reliability of the measurement results. Correspondingly, the insets in Figs. 3(a) and 3(b) display complete self-diffraction ring patterns at two characteristic intensities.

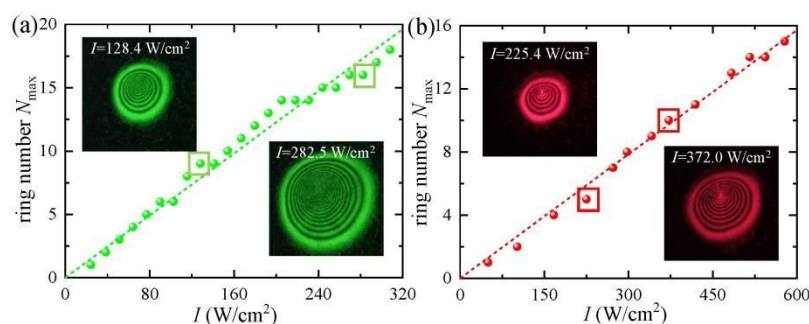


Figure 3. Intensity dependence of N_{\max} for InP nanosheets at (a) $\lambda = 532$ nm and (b) 671 nm. The corresponding insets display complete self-diffraction ring patterns at two characteristic intensities.

Quantitatively, the intensity-dependent maximum ring number N_{\max} follows a linear relationship $N_{\max} = sI$, where s is the proportionality coefficient. Dashed lines in Fig. 3 represent the optimal linear fits to the N_{\max} - I data, yielding $s = 0.061 \pm 0.001$ and 0.026 ± 0.001 cm² W⁻¹ at 532 nm and 671 nm, respectively. Using the measured s values, the nonlinear refractive indices n_2 of InP nanosheet suspensions can be directly determined by^[36,37]

$$n_2 = \frac{\lambda}{2n_0 L_{\text{eff}}} s, \quad (1)$$

where n_0 and $L_{\text{eff}} = [1 - \exp(-\alpha_0 L)]/\alpha_0$ are the linear refractive index and the effective thickness of the sample, respectively. Given the diluted InP nanosheets in NMP solvent (e.g., the mass concentration of $d_0 = 0.127 \text{ mg mL}^{-1}$), the linear refractive index n_0 of the dispersion approximates that of pure NMP solvent. Thus, we assign $n_0 = 1.468$.

Table 1. Nonlinear refractive index n_2 and third-order nonlinear susceptibility $\chi_{\text{monolayer}}^{(3)}$ of representative 2D nanomaterials at 532 nm and 671 nm wavelengths.

Wavelength	Sample	n_2 (cm ² /W)	$\chi_{\text{monolayer}}^{(3)}$ (esu)	Refs.
532 nm	VP	1.87×10^{-6}	1.08×10^{-8}	[33]
	Ga ₂ Te ₃	2.60×10^{-7}	1.12×10^{-9}	[21]
	SnS	4.53×10^{-5}	7.00×10^{-10}	[18]
	InP	1.18×10^{-6}	1.28×10^{-9}	this work
671 nm	VP	5.58×10^{-7}	3.23×10^{-9}	[33]
	MoSe ₂	6.60×10^{-6}	1.35×10^{-8}	[34]
	InSe	5.50×10^{-6}	2.87×10^{-10}	[38]
	InP	6.92×10^{-7}	7.52×10^{-10}	this work

Based on the measured s values from Fig. 3 and the known experimental parameters (e.g., $L_{\text{eff}} = 9.409 \text{ mm}$ at $\lambda = 532 \text{ nm}$), Eq. (1) yields the nonlinear refractive indices $n_2 = (1.18 \pm 0.02) \times 10^{-6} \text{ cm}^2 \text{ W}^{-1}$ at 532 nm and $(6.92 \pm 0.08) \times 10^{-7} \text{ cm}^2 \text{ W}^{-1}$ at 671 nm. For comparison, Table 1 summarizes the nonlinear refractive indices n_2 of representative nanosheet suspensions. Clearly, the n_2 values of InP nanosheets dispersed in NMP are comparable to or superior to those of VP nanosheets in NMP ($n_2 = 1.87 \times 10^{-6} \text{ cm}^2 \text{ W}^{-1}$ at 532 nm and $5.58 \times 10^{-7} \text{ cm}^2 \text{ W}^{-1}$ at 671 nm),^[33] 2D Ga₂Te₃ suspension ($2.60 \times 10^{-7} \text{ cm}^2 \text{ W}^{-1}$ at 532 nm),^[21] and suspended MoSe₂ nanoflakes ($6.60 \times 10^{-6} \text{ cm}^2 \text{ W}^{-1}$ at 671 nm).^[34]

3.5 Third-order nonlinear susceptibility of monolayer InP nanosheets

The measured n_2 reflects contributions from multilayer InP nanosheets in the dispersion, and its value is directly related to the thickness of the cuvette, the concentration of the dispersion, and other factors. Therefore, it is necessary to extract the third-order nonlinear susceptibility $\chi_{\text{monolayer}}^{(3)}$ of monolayer nanosheet. The third-order nonlinear susceptibility $\chi_{\text{monolayer}}^{(3)}$ of monolayer InP nanosheets can be calculated by^[37]

$$\chi_{\text{monolayer}}^{(3)}(\text{esu}) = \frac{n_0^2 n_2 (\text{cm}^2 \text{W}^{-1})}{0.0395 \times N_{\text{eff}}^2}, \quad (2)$$

where N_{eff} represents the effective number of InP nanosheet layers that the laser beam passes through the cuvette. Here, the solution concentration method is used to estimate the N_{eff} value,^[14] and the calculation process is as follows. The InP nanosheet dispersion a mass concentration of $d_0 = 0.127 \text{ mg mL}^{-1}$ (alternatively, a molar concentration of $\rho = 8.7 \times 10^{-4} \text{ mol L}^{-1}$) is placed in the cuvette with a volume of $V = 3 \text{ mL}$, so that the total number of original cells of InP nanosheets in the cuvette is calculated as $M = (\rho/8) \times V \times N_A = 1.96 \times 10^{17}$, where N_A is Avogadro's constant. Furthermore, since InP crystallizes the cubic crystal system with space group F-43m, the lattice constants obtained from XRD in Fig. 1(c) are $a = b = c = 5.86 \text{ \AA}$. Accordingly, the number of molecules covering a single effective layer is $m = 8.74 \times 10^{14}$. Thus, the effective number of layers for InP nanosheets is estimated to be $N_{\text{eff}} = M/m \approx 224$. In this way, the third-order nonlinear susceptibilities of monolayer InP nanosheets $\chi_{\text{monolayer}}^{(3)}$ are obtained as $(1.28 \pm 0.02) \times 10^{-9} \text{ esu}$ at $\lambda = 532 \text{ nm}$ and $(7.52 \pm 0.09) \times 10^{-10} \text{ esu}$ at $\lambda = 671 \text{ nm}$. By comparison, Table 1 also lists the third-order nonlinear susceptibilities $\chi_{\text{monolayer}}^{(3)}$ of representative 2D nanomaterials. It is shown that the $\chi_{\text{monolayer}}^{(3)}$ values of InP nanosheets are comparable to those of 2D Ga_2Te_3 ^[21] and MoSe_2 nanoflakes^[34].

The $\chi_{\text{monolayer}}^{(3)}$ value of 2D nanomaterials is correlated to the carrier mobility μ and the carrier effective mass m^* by the empirical formula^[39]

$$\chi_{\text{monolayer}}^{(3)} = 0.146 \times \sqrt{\mu}, \quad (3)$$

$$\chi_{\text{monolayer}}^{(3)} = 8.00 / \sqrt{m^*}. \quad (4)$$

Figure 4 shows the correlation between $\chi_{\text{monolayer}}^{(3)}$ and the carrier mobility μ with the effective mass m^* of InP nanosheets, where $\mu = 4800 \text{ cm}^2 \text{ V}^{-1} \text{ s}^{-1}$ and $m^* = 0.08 \times m_0$ (m_0 is the mass of free electrons), respectively.^[7] To provide a clear comparison, Fig. 4 also presents the values of other representative 2D nanomaterials including graphene,^[37] black phosphorous (BP),^[33] boron,^[40] Ga₂Te₃,^[21] MoS₂,^[21] MoSe₂,^[21] and MoTe₂.^[21]

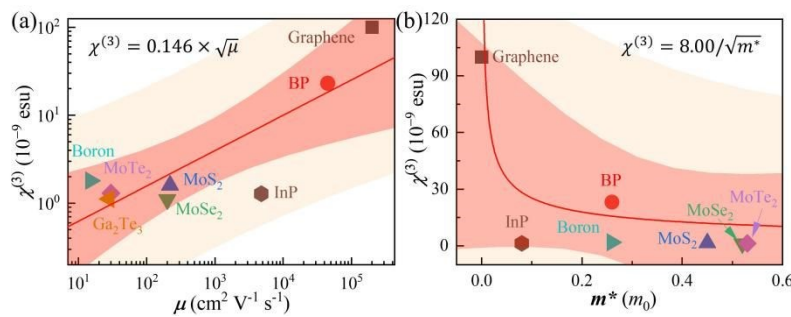


Figure 4. Correlation between $\chi_{\text{monolayer}}^{(3)}$ and (a) the carrier mobility μ with (b) the effective mass m^* .

As observed from the confidence bands (dark-colored area) and prediction bands (light-colored area) in Fig. 4, the relationship between the third-order nonlinear susceptibility $\chi_{\text{monolayer}}^{(3)}$ of monolayer InP nanosheets measured in this work and the carrier mobility μ or effective mass m^* described by the empirical formula (see Eqs. (3) or (4)) is basically consistent: its value is positively correlated with carrier mobility μ and negatively correlated with effective mass m^* . This consistency not only validates the effectiveness of the wind-chime model in interpreting the electronic coherence in InP nanosheets, but also further supports the reliability of our experimental results. Meanwhile, it highlights the potential of InP as a III-V semiconductor for future applications in nonlinear photonic devices.



3.6 Nonlinear optical properties of InP suspensions against photodegradation

The long-term stability and resistance to photodegradation of nonlinear optical materials are crucial. Therefore, we repeatedly conduct SSPM measurements on the same sample on different dates to validate the reliability of its nonlinear optical performance. In order to mitigate oxidation of the InP nanosheet dispersion following extended storage, the sample is preserved under ambient conditions at a temperature of 25 °C.

Figure 5(a) presents the maximum number of self-diffraction rings N_{\max} measured at different intensities I for the same InP nanosheet dispersion after storage durations of 1, 28, and 56 days. The results reveal two main characteristics: (i) For the sample with the same storage duration, N_{\max} increases approximately linearly with the increase of I ; (ii) For the sample with different storage durations, the values of N_{\max} show slight variations under the same intensity. For example, the inset in Fig. 5(a) displays the complete self-diffraction ring patterns obtained at an intensity of $I = 308.2 \text{ W cm}^{-2}$ after 1 day, 28 days, and 56 days of storage. It is clearly observed that the measured maximum number of rings decreases from $N_{\max} = 18$ on day 1 to 16 on day 56.

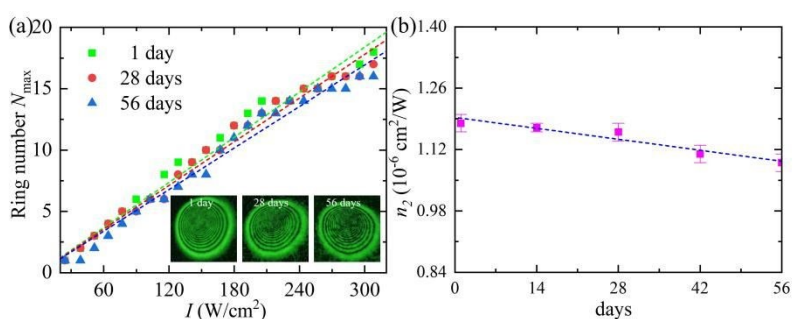


Figure 5. SSPM experimental results for the InP nanosheet dispersion after different storage days. (a) The maximum ring number N_{\max} as a function of intensity I for various storage times. The insets show the complete self-diffraction ring patterns recorded at $I = 308.2 \text{ W cm}^{-2}$ after 1, 28, and 56 days. (b) The nonlinear refractive indices n_2 derived for different storage durations.

Based on the linear dependence between N_{\max} and I measured over time, as shown

in Fig. 5(a), the nonlinear refractive indices n_2 of the InP nanosheet dispersions are calculated using Eq. (1). The results are presented in Fig. 5(b). As anticipated, the measured n_2 values exhibit a slight decrease with prolonged storage time. Specifically, the n_2 value decreases from $(1.18 \pm 0.02) \times 10^{-6} \text{ cm}^2 \text{ W}^{-1}$ on day 1 to $(1.09 \pm 0.02) \times 10^{-6} \text{ cm}^2 \text{ W}^{-1}$ on day 56, corresponding to a relative reduction of 7.6 % in the nonlinear refractive index. In short, Fig. 5 demonstrates that the nonlinear optical performance of the InP nanosheet dispersions remains largely stable, even after more than two months of storage, despite a minor degradation. Furthermore, repeated SSPM measurements confirm the sample's robust resistance to laser-induced degradation. These findings suggest that InP nanosheets, exhibiting long-term stability and high photodegradation resistance—similar to few-layer VP,^[41] Ag/VP heterojunctions,^[42] and MoP microparticles^[25]—hold significant promise for applications in nonlinear photonic devices.

4. Application of multifunctional nonlinear photonic devices

As presented in Section 3, InP nanosheets exhibit the superior electronic coherence and photostability. Leveraging the excellent SSPM behaviors of InP nanosheet dispersions, we design and demonstrate four types of nonlinear photonic devices, namely an all-optical switch, a spatially asymmetric light transmitter, a photonic diode, and an optical logic gate.

4.1 All-optical switches

Utilizing the excellent nonlinear optical properties of InP nanosheets, we construct the all-optical switching setup illustrated in Fig. 6(a). A 532 nm control beam is intensity-modulated using a half-wave plate ($\lambda/2$) followed by a G-T. This beam is then spatially overlapped with a 671 nm signal beam via a beam splitter (BS). Both beams are subsequently focused using a converging lens with a focal length of $f = 400 \text{ mm}$ onto a quartz cuvette containing a dispersion of InP nanosheets in NMP solvent. The resulting nonlinear interaction produces self-diffraction ring patterns, which are projected onto a white screen or recorded by a camera placed in the far field.

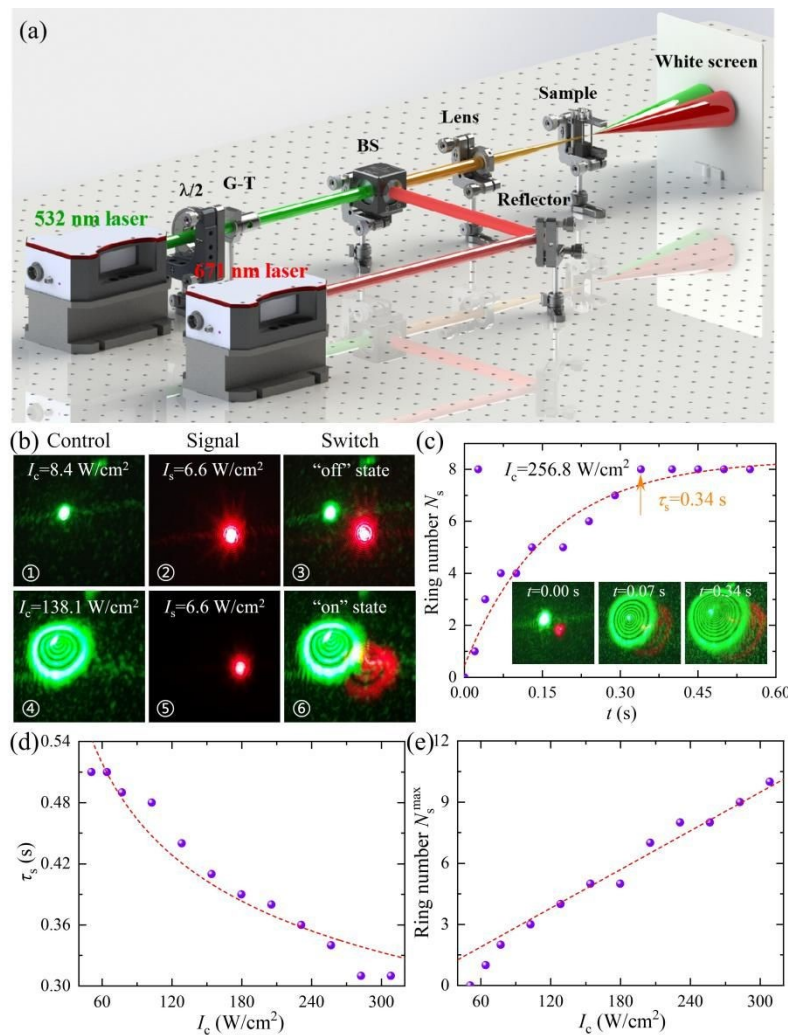


Figure 6. All-optical switch based on SSPM in InP nanosheet dispersions. (a) Schematic diagram of the experimental setup. (b) Performance demonstration of the all-optical switching. (c) The evolution of the ring number N_s of 671 nm signal beam over time t at $I_c = 256.8 \text{ W cm}^{-2}$. The insets are the self-diffraction ring patterns at three typical times. (d) I_c -dependent switching time τ_s and (e) the maximum ring number of the 671 nm signal beam N_s^{\max} .

The operating principle of the all-optical switch based on SSPM in InP nanosheets is as follows. When a strong 532 nm control beam illuminates the sample, it induces a strong nonlinear optical response, generating free carriers that modify the local refractive index. This refractive index change subsequently modulates the phase of the co-propagating weak 671 nm signal beam, leading to self-diffraction effects that

manifest as concentric rings. The presence or absence of the 532 nm control beam thus governs whether the 671 nm signal beam can exhibit a multi-ring pattern, constituting the switching action.

Using the experimental setup depicted in Fig. 6(a), the all-optical switching performance of InP nanosheet dispersions is demonstrated in Fig. 6(b). The intensity of the 671 nm signal beam is fixed at $I_s = 6.6 \text{ W cm}^{-2}$, below its SSPM excitation threshold intensity of $I_{th}^s = 21.4 \text{ W cm}^{-2}$. Initially, the 532 nm control beam is set to $I_c = 8.4 \text{ W cm}^{-2}$, also below its respective threshold intensity $I_{th}^c = 19.3 \text{ W cm}^{-2}$. At these low intensities, neither beam could generate a self-diffraction ring pattern, and the switch remained in the “off” state (see the first row of Fig. 6(b)). When the control beam intensity is increased to $I_c = 138.1 \text{ W cm}^{-2}$ (see Fig. 6b④), a green self-diffraction ring emerges, confirming that the control beam alone could excite SSPM. When both the control and signal beams are simultaneously focused onto the sample, distinct green-red self-diffraction rings appeared, indicating that the signal beam is phase-modulated via the optical nonlinearity induced by the control beam. In this state, both beams contribute to the ring patterns, and the switch is turned “on”.

To investigate the dynamic behavior of the all-optical switch, we select $I_c = 256.8 \text{ W cm}^{-2}$ of the 532 nm control beam and $I_s = 6.6 \text{ W cm}^{-2}$ of the 671 nm signal beam. The insets in Fig. 6(c) display representative self-diffraction ring patterns observed at three distinct time points. Figure 6(c) illustrates the temporal evolution of the ring number N_s generated by the 671 nm signal beam. Similar to single-beam SSPM dynamics (see Fig. 2(a)), both beams transition over time from a single spot to a multi-ring diffraction pattern. Furthermore, the rings generated by each beam undergo three characteristic stages: formation, collapse, and stabilization. To quantitatively assess the switching performance, we define two key metrics: the switching time τ_s and the maximum number of signal self-diffraction rings N_s^{\max} . The switching time τ_s is defined as the duration from when the 532 nm control beam first interacts with the sample to the moment when a complete self-diffraction ring pattern is formed by the



671 nm signal beam via the SSPM effect.

View Article Online
DOI: 10.1039/D5NR04405G

Figures 6(d) and 6(e) present the switching time τ_s and the maximum ring number of the 671 nm signal beam N_s^{\max} , respectively, as functions of the 532 nm control beam intensity I_c . It is observed that τ_s decreases linearly with increasing I_c , while N_s^{\max} exhibits a linear increase. This behavior can be attributed to the enhanced optical nonlinearity in the InP nanosheet suspension under stronger control beam illumination. A higher I_c leads to a greater nonlinear refractive index change, which accelerates the formation of the signal self-diffraction rings and results in a higher number of complete rings.

4.2 Spatially asymmetric light transmitters

Leveraging the strong SSPM response of InP nanosheets, we construct cascaded samples to investigate spatially asymmetric light propagation. The sample assembly consists of two 10 mm-thick quartz cuvettes placed in sequence, one containing a dispersion of InP nanosheets and the other of GO nanosheets in NMP, each at a mass concentration of 0.127 mg mL^{-1} . GO is selected for its compatibility with solution processing and ease of preparation. The laser beam with a wavelength of 532 nm is directed through two distinct configurations: InP followed by GO (denoted as InP/GO) and GO followed by InP (denoted as GO/InP), referred to as the forward and reverse configurations, respectively.

The working principle of spatially asymmetric light propagation based on the SSPM effect is described as follows:^[25,43] a cascaded sample is constructed by combining two nonlinear samples with significantly distinct nonlinear refractive indices. When a laser beam propagates through this cascaded assembly in both forward and reverse directions, noticeable differences emerge in both the number of self-diffraction rings and their formation dynamics. It is emphasized that the key distinction between a conventional SSPM experiment and spatially asymmetric light propagation lies in the sample configuration—the latter employs a cascaded sample rather than a single material.



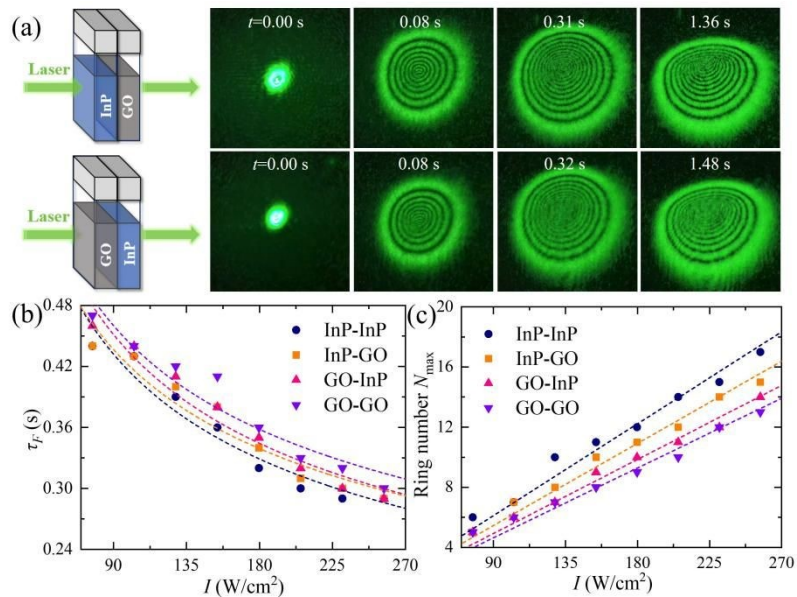


Figure 7. Spatially asymmetric light transmitter based on SSPM in InP/GO cascaded samples. (a) The self-diffraction ring patterns observed over time t in InP/GO and GO/InP cascaded samples at $I = 205.5 \text{ W cm}^{-2}$. (b) Ring formation time τ_F and (c) maximum ring number N_{\max} as a function of intensity I for InP/InP, InP/GO, GO/InP, and GO/GO cascaded samples.

Figure 7(a) illustrates the temporal evolution of self-diffraction rings for both InP/GO and GO/InP configurations at $I = 205.5 \text{ W cm}^{-2}$. In both propagation directions, the beam evolves from a central spot into a multi-ring diffraction pattern, exhibiting three characteristic stages: formation, collapse, and stabilization. At $I = 205.5 \text{ W cm}^{-2}$, the measured ring formation times are $\tau_F = 0.31 \text{ s}$ for InP/GO and 0.32 s for GO/InP, while the maximum numbers of rings are $N_{\max} = 12$ and 11, respectively. These results clearly demonstrate that reversing the beam propagation direction through the cascaded sample leads to distinct nonlinear responses, reflected in differences in both τ_F and N_{\max} . Thus, spatially asymmetric light propagation is conclusively achieved via the SSPM in InP/GO cascaded samples.

Figures 7(a) and 7(b) present the ring formation time τ_F and the maximum ring number N_{\max} as a function of intensity I for the cascaded InP/GO and GO/InP samples, along with comparative results from homogeneous InP/InP and GO/GO samples.

Similar to the behavior observed in single-material systems (see Figs. 2(c) and 3), both τ_F and N_{\max} exhibit a dependencies on intensity I across all four samples: τ_F decreases nonlinearly with I , while N_{\max} increases linearly. These results indicate that stronger optical intensities enhance the nonlinear optical response, leading to a higher number of self-diffraction rings and faster nonlinear dynamics. At a fixed intensity I , the measured τ_F values follow the order: GO/GO > GO/InP > InP/GO > InP/InP, while N_{\max} values decrease in the reverse order. This trend arises from the difference in nonlinear refractive indices between InP nanosheets ($n_2 = 1.18 \times 10^{-6} \text{ cm}^2 \text{ W}^{-1}$) and GO nanosheets ($n_2 = 9.13 \times 10^{-7} \text{ cm}^2 \text{ W}^{-1}$). The nonlinear performance of the cascaded samples (InP/GO and GO/InP) lies between those of the two homogeneous samples (InP/InP and GO/GO), resulting in intermediate τ_F and N_{\max} values. Briefly, by leveraging SSPM in cascaded InP/GO structures, we demonstrate predictable control over ring formation dynamics and self-diffraction ring number in spatially asymmetric light propagation.

The spatially asymmetric light propagation performance demonstrated in Fig. 7 can be quantitatively evaluated using the nonreciprocity factor C , which characterizes the strength of nonreciprocal nonlinear optical response, as defined by:^[43, 44]

$$C = \frac{|n_{12} - n_{21}|}{\max(n_{12}, n_{21})}. \quad (5)$$

Here, n_{12} and n_{21} denote the nonlinear refractive indices of InP/GO and GO/InP cascaded structures, respectively. A smaller value of C corresponds to a weaker nonreciprocal response. Based on the intensity-dependent N_{\max} values in Fig. 7(c), the fitted slopes are $s_{12} = 0.061 \pm 0.001 \text{ cm}^2 \text{ W}^{-1}$ for InP/GO and $s_{21} = 0.055 \pm 0.001 \text{ cm}^2 \text{ W}^{-1}$ for GO/InP. Using Eq. (1), these correspond to $n_{12} = (1.17 \pm 0.02) \times 10^{-6} \text{ cm}^2 \text{ W}^{-1}$ and $n_{21} = (1.06 \pm 0.02) \times 10^{-6} \text{ cm}^2 \text{ W}^{-1}$. The resulting value of C is 0.09, which is comparable to previously reported values such as $C = 0.098$ for CsPbI₃ quantum dots/Bi nanosheets systems.^[43] This spatially asymmetric light propagation of 2D nanomaterials offers potential for developing nonlinear photonic devices such as photonic diodes,^[34] optical logic gates,^[40] and optical isolators.^[23]

4.3 Photonic diodes



Let's examine a limiting case of Eq. (5), in which the cascaded sample enables the excitation of SSPM under forward configuration but completely suppresses it under reverse configuration. Under this condition, the nonreciprocity factor reaches $C = 1$. This behavior is analogous to the unidirectional current conduction in an electronic diode, thereby constituting a “photonic diode” mechanism that achieves spatially asymmetric light propagation—i.e., optical nonreciprocity.

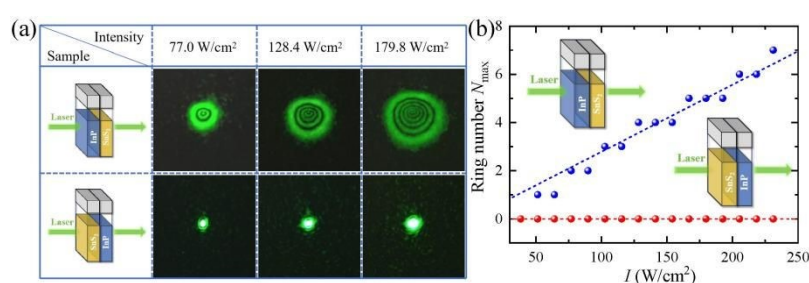


Figure 8. Photonic diode based on SSPM in InP/SnS₂ cascaded samples. (a) Self-diffraction ring patterns of the cascaded samples under different I at $\lambda = 532$ nm when the laser beam passes through the forward (InP/SnS₂) and reverse (SnS₂/InP) directions. (b) Intensity-dependent maximum ring number N_{\max} for the photonic diode.

To validate this concept, we design an SSPM experiment based on an InP/SnS₂ cascaded sample, leveraging the strong nonlinear refraction of InP nanosheets and the reverse saturable absorption of SnS₂ nanosheets. Dispersions of InP and SnS₂ nanosheets in NMP solvent—each at a mass concentration of 0.032 mg·mL⁻¹—are prepared and housed in two separate 10 mm-thick quartz cuvettes. These cuvettes are arranged side-by-side to form the cascaded sample, as schematically illustrated in Fig. 8(a). In the experimental setup, a laser beam with a wavelength of 532 nm is used. The forward configuration is defined as the beam traversing through the InP sample first and then the SnS₂ sample, while the reverse configuration refers to the beam first passing through SnS₂ and then InP.

Figure 8(a) displays the self-diffraction ring patterns of the cascaded sample at $\lambda = 532$ nm under different intensities I , with the laser beam passing through the structure in both the forward (InP/SnS₂) and reverse (SnS₂/InP) directions. The results show that

multiple concentric self-diffraction rings are observed when light travels in the forward direction through the diode. In contrast, no diffraction rings are generated under reverse illumination, demonstrating the photonic diode functionality using the InP/SnS₂ cascaded sample.

Quantitatively, Fig. 8(b) presents the intensity-dependent maximum number of self-diffraction rings N_{\max} generated by the photonic diode. When the beam passes through the cascaded sample in the forward direction (InP/SnS₂), the laser first interacts with the InP dispersion, which exhibits strong nonlinear refraction, efficiently exciting self-diffraction rings. As the light subsequently traverses the SnS₂ dispersion, the number of rings remains unchanged; however, the intensity of the SSPM rings is reduced due to the absorption behavior of SnS₂. Conversely, when the laser beam enters from the reverse direction (SnS₂/InP), it first passes through the SnS₂ dispersion. Owing to the large optical bandgap of SnS₂ ($E_g = 2.6$ eV^[45]), the laser beam with a photon energy of $h\nu = 2.33$ eV do not interact significantly with SnS₂. It is noteworthy that the reverse saturable absorption behavior of SnS₂ greatly attenuates the incident laser power,^[46] making it difficult to excite diffraction rings. Meanwhile, the reduced intensity of the light reaching the InP dispersion is insufficient to exceed the threshold for generating self-diffraction rings, as confirmed by the red curve in Fig. 8(b). Through the experimental verification shown in Fig. 8, we demonstrate that a photonic diode based on the InP/SnS₂ cascaded sample can easily achieve asymmetric light propagation for the nonreciprocity factor $C = 1$, showing promising potential for applications in all-optical information processing.

4.4 Optical logic gates

Benefiting from its excellent laser-induced electronic coherence and high photostability, InP nanosheets are promising not only for photonic diodes but also for all-optical OR logic gates. In such a logic device, a stronger laser beam modulates the propagation of a weaker one, mimicking the behavior of electronic OR gates. The logic states are defined based on optical intensity: low- and high-power levels in the input laser beams are assigned as logic “0” and “1”, respectively. The output is considered “1” whenever



self-diffraction rings are generated; otherwise, the output remains “0”.

In the optical OR gate, the system comprises two inputs—“A” (Laser A) and “B” (Laser B)—as illustrated in Figs. 9(a) and 9(b), and a single output “Y” (where $Y = A + B$). The output “Y” attains a high logic level “1” if at least one of the inputs “A” or “B” is at the high level “1”. Conversely, only when both “A” and “B” are at the low logic level “0” does the output “Y” remain at “0”. These results are consistent with the waveform depicted in Fig. 9(c).

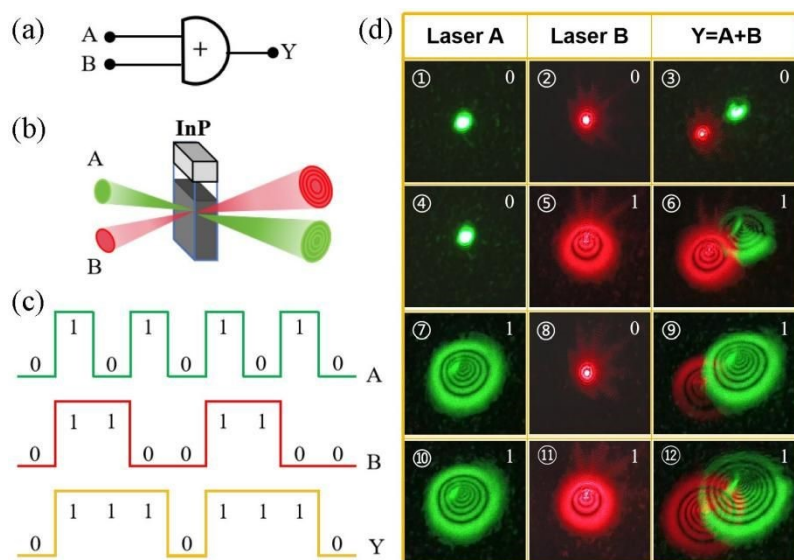


Figure 9. All-optical logic gate based on InP nanosheet dispersions. (a) Symbol of the logical OR gate. (b) Schematic diagram of the optical modulation system. (c) Input and output waveforms for the OR logic operation. (d) Experimental results of the logic OR gate at $\lambda = 532$ nm and 671 nm.

The optical logic gate shares similarities with the all-optical switch described in Subsection 4.1, as both employ two laser beams with different photon energies. However, unlike the all-optical switch where control and signal beams are strictly defined, the two beams in the logic gate are mutually modulatable and interchangeable, with adjustable intensities. In our experiments, two laser beams with wavelengths of $\lambda = 532$ nm and 671 nm are incident on the InP nanosheet dispersion, and the resulting self-diffraction rings serve as the input optical signals. When both input beams “A” and



“B” are at a low intensity level (“0”), they do not interact sufficiently with the sample due to their low intensity, failing to produce any SSPM rings on the far-field screen (see Fig. 9d①-③). If Laser A remains at “0” while Laser B is increased to a high intensity (“1”), the output “Y” switches to a high level (“1”), consistent with the OR logic operation “0 + 1 = 1”. As revealed in Fig. 9d④-⑥, when the high-intensity red laser beam passes through the InP nanosheet dispersion, it modifies the spatial refractive index distribution of the medium, inducing an additional nonlinear phase shift. This change subsequently enables the cross-coupled weaker beam (Laser B) to generate self-diffraction ring patterns. Conversely, the stronger beam (Laser A) can also modulate the weaker beam (Laser B), as demonstrated in Fig. 9d⑦-⑨. Similarly, when both beams are at high intensity (logic “1”), clearly visible self-diffraction rings with larger diameters are observed, consistent with the results presented in Fig. 9d⑩-⑫. In a word, the output measurements under the four states illustrated in Fig. 9d demonstrate the successful implementation of an all-optical OR logic gate, confirming the feasibility of performing logic operations purely through optical control without intermediate electronic conversion.

5. Conclusions

In summary, we have prepared and characterized InP nanosheet dispersions, investigated their SSPM behaviors, and demonstrated their applications in multifunctional nonlinear photonic devices. Through analysis of the dynamics of self-diffraction ring formation, the ring formation time τ_F and the third-order nonlinear susceptibility of monolayer InP nanosheets $\chi_{\text{monolayer}}^{(3)}$ are determined to be approximately 0.3 s and 10^{-9} esu, respectively—values comparable to those of typical 2D nanomaterials. The dominant mechanism underlying the light-InP interactions in the SSPM is laser-induced electron coherence, with thermal effect playing a secondary role. Repeated tests conducted on samples aged nearly two months confirm that its nonlinear optical response remains generally stable, indicating good photophysical



stability of the InP nanosheets. Leveraging the superior electronic coherence and photostability of InP nanosheets, we have designed and demonstrated four types of nonlinear photonic devices: all-optical switches using InP nanosheets, spatially asymmetric light transmitters based on InP/GO cascaded structure, photonic diodes employing InP/SnS₂ cascaded systems, and optical logic gates utilizing InP nanosheets. This work not only addresses a significant gap in the third-order nonlinear optical research of III-V semiconductor nanomaterials, but also opens new pathways for developing high-performance multifunctional nonlinear photonic devices. Finally, the following remarks are made on the multifunctional nonlinear photonic devices based on SSPM in InP nanosheets: the advantages include a simple device structure, no need for external electronic modulation, and ease of fabrication; the drawback lies in the sub-second-scale ring formation time due to the wind-chime-like reorientation of InP nanosheets under an external field, which leads to a relatively slow response of these devices.

Acknowledgements

This work was supported by the National Nature Science Foundation of China (Grant Nos. 12474323, 12074066).

Reference

- [1] J. A. del Alamo, *Nature*, 2011, **479**, 317-323.
- [2] Y. Zhu, V. Raj, Z. Li, H. H. Tan, C. Jagadish and L. Fu, *Adv. Mater.*, 2021, **33**, 2105729.
- [3] H. Wang, D. Zhou, R. Zhang, D. Lu, L. Zhao, H. Zhu, W. Wang and C. Ji, *Chin. Phys. Lett.*, 2015, **32**, 084203.
- [4] S. Mokkapati and C. Jagadish, *Mater. Today*, 2009, **12**, 22-32.
- [5] X. Wang, L. Xu, Y. Jiang, Z. Yin, C. C. S. Chan, C. Deng and R. A. Taylor, *J. Semicond.*, 2019, **40**, 071906.
- [6] J. Liu, H. Nie, B. Yan, K. Yang, H. Yang, V. Khayrudinov, H. Lipsanen, B. Zhang and J. He, *Photonics Res.*, 2020, **8**, 1035-1041.



[7] W. Walukiewicz, J. Lagowski, L. Jastrzebski, P. Rava, M. Lichtensteiger, Gatos and H. C. Gatos, *J. Appl. Phys.*, 1980, **51**, 2659-2668.

[8] C. Jacoboni, C. Canali, G. Ottaviani and A. A. Quaranta, *Solid-State Electron.*, 1977, **20**, 77-89.

[9] G. Chen, M. Wang, W. Yang, M. Tan, Y. Wu, P. Dai, Y. Huang and S. Lu, *J. Semicond.*, 2017, **38**, 124004.

[10] V. Jain, M. Heurlin, E. Barrigon, L. Bosco, A. Nowzari, S. Shroff, V. Boix, M. Karimi, R. J. Jam, A. Berg, L. Samuelson, M. T. Borgström, F. Capasso and H. Pettersson, *ACS Photonics*, 2017, **4**, 2693-2698.

[11] Y. Zhang, Y. Ji, A. Khaliq, H. Chai, M. Ali, A. Qadir, I. Saeed, X.-G. Yang and S. Du, *Appl. Phys. A-Mater.*, 2024, **130**, 531.

[12] M. D. Dvorak and B. L. Justus, *Opt. Commun.*, 1995, **114**, 147-150.

[13] H. Wang, D. Wang, G. Chen and H. Liu, *Chin. Phys. Lett.*, 2007, **24**, 2600-2602.

[14] Y. Wu, Q. Wu, F. Sun, C. Cheng, S. Meng and J. Zhao, *Proc. Natl. Acad. Sci. U.S.A.*, 2015, **112**, 11800-11805.

[15] Y. Liao, C. Song, Y. Xiang and X. Dai, *Ann. Phys.-Berlin*, 2020, **532**, 2000322.

[16] L. Wu, X. Yuan, D. Ma, Y. Zhang, W. Huang, Y. Ge, Y. Song, Y. Xiang, J. Li and H. Zhang, *Small*, 2020, **16**, 2002252.

[17] Y. Gao, Y. Hu, C. Ling, G. Rui, J. He and B. Gu, *Nanoscale*, 2023, **15**, 6225-6233.

[18] L. Wu, Z. Xie, L. Lu, J. Zhao, Y. Wang, X. Jiang, Y. Ge, F. Zhang, S. Lu, Z. Guo, J. Liu, Y. Xiang, S. Xu, J. Li, D. Fan and H. Zhang, *Adv. Opt. Mater.*, 2018, **6**, 1700985.

[19] Y. Shan, J. Tang, L. Wu, S. Lu, X. Dai and Y. Xiang, *J. Alloys Compd.*, 2019, **771**, 900-904.

[20] L. Wu, X. Jiang, J. Zhao, W. Liang, Z. Li, W. Huang, Z. Lin, Y. Wang, F. Zhang, S. Lu, Y. Xiang, S. Xu, J. Li and H. Zhang, *Laser Photonics Rev.*, 2018, **12**, 1800215.

[21] A. Pramanik, P. Kumbhakar, A. Dey, K. Mondal, D. Banerjee, V. R. Soma, P. Kumbhakar and C. S. Tiwary, *ACS Appl. Opt. Mater.*, 2023, **1**, 1634-1642.

[22] L. Wu, W. Huang, Y. Wang, J. Zhao, D. Ma, Y. Xiang, J. Li, J. S. Ponraj, S. C. Dhanabalan and H. Zhang, *Adv. Funct. Mater.*, 2019, **29**, 1806346.

[23] L. Wu, Y. Zhang, X. Yuan, F. Zhang, W. Huang, D. Ma, J. Zhao, Y. Wang, Y. Ge,



H. Huang, N. Xu, J. Kang, Y. Xiang, Y. Zhang, J. Li and H. Zhang, *Appl. Mater. Today*, 2020, **19**, 100589.

[24] J. Xu, C. Zhang, Y. Wang, M. Wang, Y. Xu, T. Wei, Z. Xie, S. Liu, C.-K. Lee, X. Hu, G. Zhao, X. Lv, H. Zhang, S. Zhu and L. Zhou, *Nat. Commun.*, 2024, **15**, 1726.

[25] D. Weng, C. Ling, Y. Gao, G. Rui, L. Fan, Q. Cui, C. Xu and B. Gu, *Laser Photonics Rev.*, 2025, **19**, 2401587.

[26] S. K. Nayak, M. S. Ahmed, R. Murali, B. Bhavani, S. Prasanthkumar, L. Giribabu and S. S. K. Raavi, *J. Mater. Chem. C*, 2024, **12**, 9841-9852.

[27] A. Ciesielski and P. Samorì, *Chem. Soc. Rev.*, 2014, **43**, 381-398.

[28] P. Huang, X. Liu, G. Jin, F. Liu, H. Shen and H. Li, *Adv. Opt. Mater.*, 2023, **11**, 2300612.

[29] Y. Niu, S. Ma, H. Dong, Z. Yang, X. Hao, B. Han, S. Wu, H. Dong and B. Xu, *Chin. J. Lumin.*, 2024, **45**, 779-793.

[30] J. Tauc, R. Grigorovici and A. Vancu, *Phys. Stat. Sol.*, 1966, **15**, 627-637.

[31] T. Davarzani, A. Bakhshayeshi, I. Motie and R. Taghavimendi, *Physica E*, 2023, **147**, 115599.

[32] H. Sahin, S. Cahangirov, M. Topsakal, E. Bekaroglu, E. Akturk, R. T. Senger and S. Ciraci, *Phys. Rev. B*, 2009, **80**, 155453.

[33] X. Xu, M. Wang, Y. Zhang, Q. Li, W. Niu, Y. Yang, J. Zhao and Y. Wu, *Laser Photonics Rev.*, 2024, **18**, 2300930.

[34] K. Sk, B. Das, N. Chakraborty, M. Samanta, S. Bera, A. Bera, D. S. Roy, S. K. Pradhan, K. K. Chattopadhyay and M. Mondal, *Adv. Opt. Mater.*, 2022, **10**, 2200791.

[35] J. N. Heyman, D. Bell and T. Khumalo, *Appl. Phys. Lett.*, 2006, **88**, 162104.

[36] S. D. Durbin, S. M. Arakelian and Y. R. Shen, *Opt. Lett.*, 1981, **6**, 411-413.

[37] R. Wu, Y. Zhang, S. Yan, F. Bian, W. Wang, X. Bai, X. Lu, J. Zhao and E. Wang, *Nano Lett.*, 2011, **11**, 5159-5164.

[38] Y. Liao, Y. Shan, L. Wu, Y. Xiang and X. Dai, *Adv. Opt. Mater.*, 2020, **8**, 1901862.

[39] L. Hu, F. Sun, H. Zhao and J. Zhao, *Opt. Lett.*, 2019, **44**, 5214-5217.

[40] C. Song, Y. Liao, Y. Xiang and X. Dai, *Sci. Bull.*, 2020, **65**, 1030-1038.

[41] L. Zhou, J. Kang, Y. Dong, Y. Wang, Y. Li, H. Huang, S. Xiao, Y. Wang and J.



He, *Nano Res.*, 2023, **16**, 5843-5849.

[View Article Online](#)
DOI: 10.1039/D5NR04405G

[42] Y. Gao, C. Ling, D. Weng, G. Rui, J. He, Q. Cui, C. Xu and B. Gu, *Nanoscale*, 2024, **16**, 18046-18055.

[43] L. Wu, K. Chen, W. Huang, Z. Lin, J. Zhao, X. Jiang, Y. Ge, F. Zhang, Q. Xiao, Z. Guo, Y. Xiang, J. Li, Q. Bao and H. Zhang, *Adv. Opt. Mater.*, 2018, **6**, 1800400.

[44] L. Wu, Y. Dong, J. Zhao, D. Ma, W. Huang, Y. Zhang, Y. Wang, X. Jiang, Y. Xiang, J. Li, Y. Feng, J. Xu and H. Zhang, *Adv. Mater.*, 2019, **31**, 1807981.

[45] G. L. Ye, Y. J. Gong, S. D. Lei, Y. M. He, B. Li, X. Zhang, Z. H. Jin, L. L. Dong, J. Lou, R. Vajtai, W. Zhou and P. M. Ajayan, *Nano Res.*, 2017, **10**, 2386-2394.

[46] J. Wu, Y. Tao, X. Wu and Y. Chun, *J. Alloys Compd.*, 2017, **713**, 38-45.



Data Availability Statement

[View Article Online](#)
DOI: 10.1039/D5NR04405G

Oct. 20, 2025

The data related to this study are included in the article. The author ensures that the data presented in the article are accurate and reliable. Any additional data are available from the corresponding author on a reasonable request.

